Extratropical Cyclones in Idealized Simulations of Changed Climates

STEPHAN PFAHL

Institute for Atmospheric and Climate Science, ETH Zurich, Zurich, Switzerland

PAUL A. O'GORMAN

Department of Earth, Atmospheric and Planetary Sciences, Massachusetts Institute of Technology, Cambridge, Massachusetts

MARTIN S. SINGH

Department of Earth and Planetary Sciences, Harvard University, Cambridge, Massachusetts

(Manuscript received 1 December 2014, in final form 22 July 2015)

ABSTRACT

Cyclones are a key element of extratropical weather and frequently lead to extreme events like wind storms and heavy precipitation. Understanding potential changes of cyclone frequency and intensity is thus essential for a proper assessment of climate change impacts. Here the behavior of extratropical cyclones under strongly varying climate conditions is investigated using idealized climate model simulations in an aquaplanet setup. A cyclone tracking algorithm is applied to assess various statistics of cyclone properties such as intensity, size, lifetime, displacement velocity, and deepening rates. In addition, a composite analysis of intense cyclones is performed. In general, the structure of extratropical cyclones in the idealized simulations is very robust, and changes in major cyclone characteristics are relatively small. Median cyclone intensity, measured in terms of minimum sea level pressure and lower-tropospheric relative vorticity, has a maximum in simulations with global mean temperature slightly warmer than present-day Earth, broadly consistent with the behavior of the eddy kinetic energy analyzed in previous studies. Maximum deepening rates along cyclone tracks behave similarly and are in agreement with linear quasigeostrophic growth rates if the effect of latent heat release on the stratification is taken into account. In contrast to moderate cyclones, the relative vorticity of intense cyclones continues to increase with warming to substantially higher temperatures, and this is associated with enhanced lower-tropospheric potential vorticity anomalies likely caused by increased diabatic heating. Moist processes may, therefore, lead to the further strengthening of intense cyclones in warmer climates even if cyclones weaken on average.

1. Introduction

Extratropical cyclones are an essential component of the global atmospheric circulation (e.g., Chang et al. 2002). They transport heat and moisture poleward, are associated with a substantial part of the synoptic weather variability in the extratropics, and can cause extreme winds and precipitation with huge impacts on society (Donat et al. 2010; Pfahl and Wernli 2012). The frequent passage of cyclones in the storm-track regions is related to local maxima in the transient atmospheric variability on time scales of a few days (Blackmon et al. 1977; Wallace et al. 1988). Storm tracks have widely been studied based on measures of this variability, like bandpass-filtered variances of wind velocity or eddy kinetic energy (EKE) (Hoskins and Hodges 2002; Chang et al. 2002; O'Gorman and Schneider 2008a; O'Gorman 2010; Chang et al. 2013). This approach yields an objective identification of storm tracks and can easily be applied to large reanalysis and climate model datasets. A complementary perspective providing additional insights has been obtained from feature-based methods that identify and track individual cyclones (Murray and Simmonds 1991; Hoskins and Hodges 2002; Wernli and Schwierz 2006; Lambert and Fyfe 2006;

Corresponding author address: Stephan Pfahl, Institute for Atmospheric and Climate Science, ETH Zurich, Universitaetstrasse 16, 8092 Zurich, Switzerland.
E-mail: stephan.pfahl@env.ethz.ch

DOI: 10.1175/JCLI-D-14-00816.1

© 2015 American Meteorological Society

Bengtsson et al. 2009; Ulbrich et al. 2009; Zappa et al. 2013). Such cyclone tracking approaches allow for a direct assessment of the physical processes in and potential impacts of individual weather systems. However, they are based on certain subjective definitions, and some results may depend on the specific implementation (Raible et al. 2008; Neu et al. 2013).

Changes in the location and intensity of storm tracks and cyclones with global warming can have important consequences for regional weather and climate in the extratropics. Various studies have investigated such potential changes in general circulation model (GCM) simulations of projected future climates (Hall et al. 1994; Knippertz et al. 2000; Bengtsson et al. 2006; Lambert and Fyfe 2006; Pinto et al. 2007; Ulbrich et al. 2009; Bengtsson et al. 2009; O'Gorman 2010; Catto et al. 2011; Zappa et al. 2013; Chang 2013). Several of these studies have found modest decreases in cyclone frequency and a poleward shift with warming, but most aspects of the storm-track response to global warming remain uncertain given model biases and intermodel differences in future projections (Ulbrich et al. 2009; Chang et al. 2013; Zappa et al. 2013; Feser et al. 2015). A more fundamental understanding of the physical mechanisms leading to changes in cyclone properties in different climates is thus required, and a promising way to obtain this is through idealized model experiments. Previous studies have, for instance, used artificial sea surface temperature (SST) perturbations in aquaplanet GCMs to investigate changes in poleward energy transport (Caballero and Langen 2005) or storm-track intensity and position (e.g., Brayshaw et al. 2008; Lu et al. 2010). Graff and LaCasce (2014) performed similar experiments with SST perturbations in a full GCM with more realistic boundary conditions, looking also at individual cyclone intensities and trajectories. Caballero and Hanley (2012) studied the role of cyclones in poleward moisture transport in aquaplanet simulations with altered CO_2 concentrations. O'Gorman and Schneider (2008a) investigated the response of the storm tracks to strongly different climate conditions in aquaplanet simulations with an idealized GCM by varying the longwave optical thickness in the radiation scheme of the GCM. They found that the EKE in different climates scales with the dry mean available potential energy (MAPE), and that combined changes of horizontal temperature gradients, vertical stability, and tropopause height lead to nonmonotonic variations of MAPE with global mean temperature (see also Held 1993; Schneider et al. 2010). O'Gorman (2011) took latent heat release into account in the calculation of MAPE and found that while this increased the MAPE values by more in warmer climates, it only led to modest changes in the scaling of MAPE across climates. Similar scaling between EKE and MAPE was also found in simulations with comprehensive climate models (O'Gorman 2010). However, this scaling behavior of EKE and MAPE does not necessarily apply to individual cyclones. In particular, the EKE includes contributions from both cyclones and anticyclones, and it is possible that the role of moisture and latent heating (LH) is more pronounced for certain classes of cyclones (cf. Plant et al. 2003) or for deepening rates rather than measures of intensity. LH has been shown to be important for cyclone intensification in theoretical studies (e.g., Emanuel et al. 1987), idealized life cycle experiments (Boutle et al. 2011; Booth et al. 2013; Schemm et al. 2013), and various case studies (e.g., Kuo et al. 1991; Stoelinga 1996; Ahmadi-Givi et al. 2004), but climatologically the role of moisture for the statistical distribution of cyclone intensities is less clear. Quantifying the effects of LH is difficult because of the relatively small spatial scales of moist processes, which can only be accurately represented with high model resolution (Willison et al. 2013).

In this study, idealized GCM simulations similar to those of O'Gorman and Schneider (2008a) are used together with a cyclone tracking scheme (Wernli and Schwierz 2006) to investigate the characteristics of extratropical cyclones in different climates. The overall aim of the study is to extend the analysis of cyclone statistics to a wide range of climates (from very cold to very warm) while comparing the results with Eulerian statistics (such as EKE) and with theory. Deepening rates are considered in addition to measures of cyclone structure, propagation, and intensity. The resolution dependence of moist processes is estimated based on simulations with varying spectral resolution (from T42 to T170, typical for global climate simulations). After introducing the idealized GCM and tracking scheme in section 2, the climate dependence of various statistics of cyclone properties is discussed in section 3. Intense cyclones are studied in more detail with the help of a composite technique in section 4.

2. Simulations and cyclone tracking

a. Idealized GCM

Simulations with an idealized GCM in an aquaplanet setup are performed, similar to those of O'Gorman and Schneider (2008a). The idealized GCM is similar to that of Frierson et al. (2006), with details as in O'Gorman and Schneider (2008b). It includes a slab mixed layer ocean, a simple quasi-equilibrium convection scheme (following Frierson 2007), and a large-scale microphysical parameterization taking only the vapor–liquid phase

transition into account. Insolation at the top of the atmosphere is prescribed as a function of latitude with no diurnal or seasonal cycle, leading to a statistically steady, zonally and hemispherically symmetric climate. The two-stream gray radiation scheme, which is applied for the parameterization of longwave radiation, uses an optical thickness $\tau = \alpha\tau_{\mathrm{ref}}$, where τ_{ref} is a fixed function of latitude and pressure (O'Gorman and Schneider 2008b). In a series of 15 simulations, the scaling parameter α is varied between 0.4 and 6.0, leading to strongly different climates with global mean near-surface air temperatures T_G between 270 and 316 K. The reference simulation with $\alpha = 1.0$ has a global mean surface air temperature similar to present-day earth. These changes in optical thickness are used to represent variations in longwave absorbers like carbon dioxide and water vapor; radiative water vapor feedbacks and radiative effects of clouds are not taken into account. While the model accounts for the effects of changing water vapor on latent heat release and on density (via the virtual temperature), it does not include changes in the mass of the atmospheric column due to evaporation and precipitation. These changes in mass can be important for strongly precipitating tropical systems in the current climate (Lackmann and Yablonsky 2004), and not including them may affect our results also in the extratropics, in particular in warmer climates. The standard set of simulations is performed with a spectral horizontal resolution of T85 and 30 vertical sigma levels. To investigate the effect of horizontal resolution, simulations for $\alpha = 0.4$, 1.0, and 4.0 with resolutions of T42, T127, and T170, are also analyzed. Furthermore, T85 simulations for $\alpha = 1.0$ are performed with different numbers of vertical levels (20, 40, 60, and 90), but these are very similar to the reference simulation and are not discussed any further. Simulations with resolutions higher than T42 are spun up for 300 days using the end of a lower-resolution simulation as an initial condition (interpolated to the higher-resolution model grid). T42 simulations are spun up from an isothermal state for 800 days. Statistics are collected four times daily for 300 days in all simulations except $\alpha = 0.4$, 1.0, and 4.0 at T85 resolution, which are run for 900 days. Because of the steady and spatially symmetric climate, this yields statistically robust results.

b. Cyclone identification and tracking

Cyclones are identified and tracked based on sea level pressure (SLP) fields, using an updated version of the algorithm of Wernli and Schwierz (2006) [very similar to Pfahl and Wernli (2012)]. A cyclone is defined as an area bounded by the outermost closed SLP contour not longer than 7500 km containing one or several SLP minima. The deepest minimum is kept and used for cyclone tracking. Successive SLP minima are connected to form a cyclone track if they occur within a specific search area that takes the previous cyclone trajectory into account. Only cyclone tracks with a minimum lifetime of 24 h and an SLP difference of at least 1 hPa between the minimum and outermost contour at each time step are used in the statistical analysis. In the following, the term cyclone is used synonymously with "cyclone track" (i.e., it refers to the whole life cycle of a specific storm, except when cyclone frequency is calculated as in Fig. 3). Most analyses are done for extratropical cyclones whose SLP minimum (along the track) is located between 30° and 80° latitude in either hemisphere. A cyclone dataset based on the ERA-Interim data from the European Centre for Medium-Range Weather Forecasts (Dee et al. 2011) is used for comparison, which has been obtained with the same tracking algorithm for the period 1979–2012 [an updated version of the dataset used by Pfahl and Wernli (2012)]. Although it is not a priori clear that results on cyclone statistics obtained from one single tracking algorithm are generally representative, it has been shown that structural differences between different tracking schemes mainly affect the identification of weak cyclones and that the response of intense systems to greenhouse gas forcing is typically robust (Neu et al. 2013; Ulbrich et al. 2013).

For a more detailed analysis of intense cyclones, composite fields in a cyclone-centered coordinate system are compiled (cf. Bengtsson et al. 2009; Catto et al. 2010). The 100 extratropical cyclones with lowest minimum SLP per 300 days of simulation are selected (i.e., for the longer simulations with $\alpha = 0.4$, 1.0, and 4.0 at T85 resolution, 300 cyclones are analyzed). Different meteorological fields (SLP, lower-tropospheric relative vorticity, the temperature anomaly relative to the mean extratropical temperature vertically interpolated to the 850-hPa level, and precipitation) at the time of minimum SLP of each cyclone are interpolated to a radial coordinate system centered on the cyclone center. These fields are then averaged over all selected cyclones from a specific simulation. Note that here these fields are not rotated prior to averaging. Cyclone fields from the Southern Hemisphere are flipped in the meridional direction, such that the composites refer to Northern Hemisphere cyclones. A similar composite analysis for idealized aquaplanet simulations has been performed by Caballero and Hanley (2012), who focused on the effect of cyclones on poleward moisture transport. In addition, vertical profiles of potential vorticity (PV) anomalies are composed for the selected intense extratropical cyclones following Campa and Wernli (2012). Since we are

interested in synoptic-scale structures, Ertel PV is approximated by

$$\mathrm{PV} \approx -g\left[\left(-\frac{\partial u}{\partial y}+\frac{\partial v}{\partial x}+f\right)\frac{\partial \theta}{\partial p}+\frac{\partial u}{\partial p}\frac{\partial \theta}{\partial y}-\frac{\partial v}{\partial p}\frac{\partial \theta}{\partial x}\right], \qquad (1)$$

where θ denotes potential temperature, u and v are the horizontal wind components, f is the Coriolis parameter, p is pressure, and g is the acceleration due to gravity. The horizontal derivatives in Eq. (1) are at constant pressure, and these were calculated from the horizontal derivatives at constant sigma by including additional terms to account for variations in surface pressure (Arakawa and Suarez 1983). PV anomalies are calculated with respect to a local climatology on each sigma level. These anomalies are averaged in a radius of 350 km around each cyclone center at the time of minimum SLP [a larger radius than in Campa and Wernli (2012) is used here because of the coarser spatial resolution]. The median PV anomaly as well as the 5th and 95th percentiles over all selected cyclones are then determined on each vertical level. For comparison, this PV analysis is also performed for cyclones with moderate intensity: 100 extratropical cyclones for every 300 days of simulations are selected with minimum SLP closest to the median value from the respective simulation.

c. *Mean changes in temperature and wind*

Before analyzing variations in cyclone occurrence and properties, changes in the mean temperature and circulation structure with climate in our simulations are reviewed. Figure 1 shows the zonal mean temperature and zonal wind from the coldest simulation (T_G = 270 K), the reference simulation (T_G = 288 K), and two simulations with higher global mean surface air temperatures (T_G = 300 and 311 K). In the reference simulation (Fig. 1b), wind maxima corresponding to subtropical and midlatitude jets can be distinguished, and the dynamical tropopause slopes down from above 200 hPa in the tropics to below 400 hPa at the poles. The pole-to-equator temperature difference is 45 K. The near-surface temperature gradient is enhanced in the cold simulation (Fig. 1a), while in the warmer climates (Figs. 1c,d), the meridional temperature gradient is reduced at low levels, but enhanced in the middle to upper troposphere, in particular in the subtropics. This is associated with a strengthening of the upper-level jet between 30° and 40° latitude and reduced wind velocities in the midlatitudes.

To facilitate the comparison with results from comprehensive GCMs, the zonal mean temperature difference between the simulation with α = 1.4 and the reference simulation is shown in Fig. 2. The global mean temperature change of 6 K between these simulations is slightly greater than the upper end of the projected warming from models of phase 5 of CMIP (CMIP5) at the end of the century (Knutti and Sedlacek 2013). In the lower troposphere, our simulations feature an amplified warming in polar regions compared to the tropics and subtropics, associated with a decreased near-surface temperature gradient. This polar amplified warming occurs even without sea ice loss, and increased poleward energy transport (O'Gorman and Schneider 2008b) as well as different lapse rate changes and Planck feedbacks at low and high latitudes are likely to be contributing factors (e.g., Pithan and Mauritsen 2014). In contrast to that, upper-tropospheric warming is larger in the tropics (see again Fig. 2), which is due to the tendency for the tropical atmosphere to maintain moist adiabatic lapse rates and the decrease in the moist-adiabatic lapse rate with warming. Accordingly, the upper-level meridional temperature gradient and the strength of the subtropical jet are enhanced, consistent with climate projections from full GCMs (e.g., Yin 2005; Grise and Polvani 2014). Apart from that, changes in zonal wind velocity are relatively small (cf. the black and green contours in Fig. 2). Interestingly, there is no poleward shift of the midlatitude jet, which is predicted by some comprehensive GCMs, but not consistently in all seasons and both hemispheres (see again Grise and Polvani 2014). Rather, the regions with strongest westerlies in the midlatitudes shift slightly equatorward throughout the whole troposphere. This equatorward shift may relate to an increased importance in warmer climates of the region of anomalous eddy momentum flux divergence discussed by Birner et al. (2013), and the exact mechanisms are being investigated.

3. Cyclone statistics

a. *Frequency*

The zonal mean cyclone frequency, averaged over both hemispheres at each latitude, is shown in Fig. 3 for four simulations spanning the range of simulated climates. This cyclone frequency indicates the percentage of time during which a specific grid point is located within a closed pressure contour that defines the outer margin of a cyclone (cf. Wernli and Schwierz 2006). Note that for this calculation, cyclones with a lifetime of less than 1 day are also taken into account. Nevertheless, very similar curves are obtained if only the positions of the cyclone centers are gridded (as in, e.g., Bengtsson et al. 2006; Neu et al. 2013) and if only cyclones living at least 24 h are considered (not shown). In the reference simulation (solid line), the zonal mean cyclone

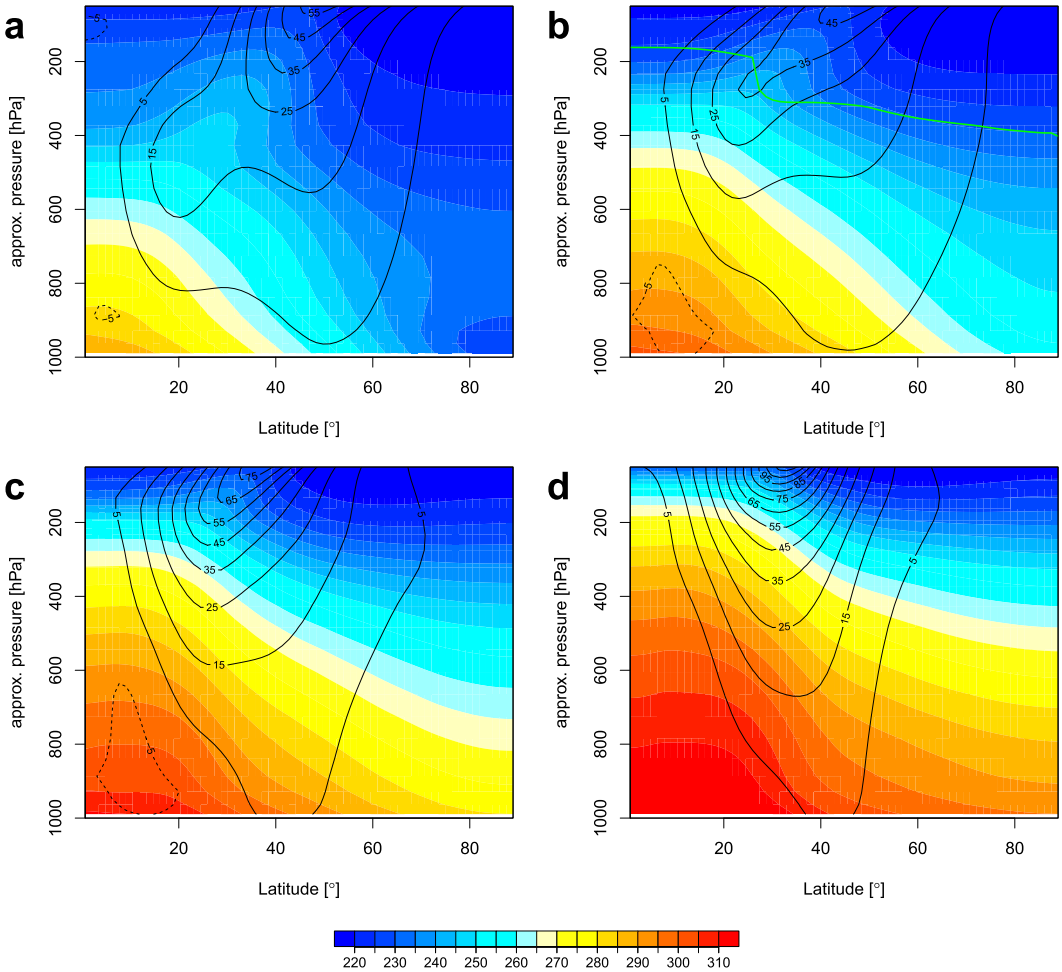

FIG. 1. Zonal mean temperature (color shading; K) and zonal wind speed (contours, interval of 10 m s^{-1}, starting from −5 m s^{-1}, negative contour dashed) in T85 simulations with varying global mean surface air temperatures T_G (resulting from changes in the optical thickness α): (a) $T_G = 270$ K ($\alpha = 0.4$), (b) $T_G = 288$ K ($\alpha = 1.0$), (c) $T_G = 300$ K ($\alpha = 2.0$), and (d) $T_G = 311$ K ($\alpha = 4.0$). The green line in (b) shows the pressure of the dynamical tropopause, which is defined as the ±2-PVU isosurface or the 380-K θ isosurface (whichever is lower). Fields from both hemispheres have been averaged. Data are plotted on vertical sigma levels, and the approximate pressure at the vertical axis refers to a surface pressure of 1000 hPa.

frequency has a maximum of almost 25% at a latitude slightly poleward of 60°, and a frequency of 10% is found around 40° latitude. This is very similar to the interhemispheric and zonal average cyclone frequency from ERA-Interim (shown as a red line in Fig. 3), in spite of the many simplifications in the idealized model. Deviations may be partly related to topography, which leads to reduced cyclone frequencies south of about 70°S in the reanalysis, and to the fact that, in contrast to ERA-Interim, almost no tropical cyclones equatorward of 20° are identified in the GCM. In the cold climate with $T_G = 270$ K (dotted line) the high-latitude frequency peak is of comparable magnitude as in the reference simulation, and a secondary maximum is found at around 30°. For warmer climates (dashed and dashed–dotted lines) the cyclone frequency peak is shifted equatorward, and the latitude band with frequencies above 10% becomes narrower. Only on the equatorward side of this band, a clear poleward shift can be observed with increasing temperature, whereas at high latitudes, cyclone frequencies are reduced in warm climates, in line with the decreased baroclinicity and westerly wind velocities in these regions (see again Fig. 1). As with the peak in cyclone frequency, the peaks in column-integrated EKE and the surface westerlies both move equatorward with warming over part of the range of climates (see section 2c), although the near-surface EKE maximum does shift poleward (Schneider et al. 2010). The equatorward shift is interesting, but poleward shifts of the storm tracks have been identified

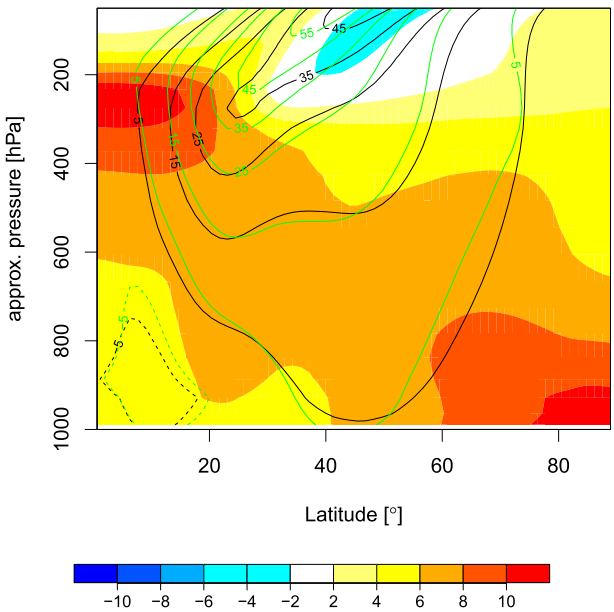

FIG. 2. Zonal mean temperature difference (K) between T85 simulations with $T_G = 294$ K ($\alpha = 1.4$) and $T_G = 288$ K ($\alpha = 1.0$). Black and green contours show the zonal mean zonal wind speed (intervals of 10 m s^{-1}, starting from −5 m s^{-1}, negative contour dashed) from the simulations with $T_G = 288$ and 294 K, respectively.

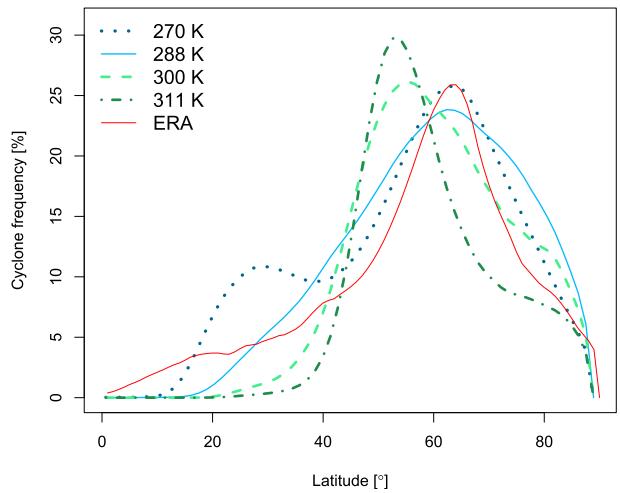

FIG. 3. Zonal mean cyclone frequency in T85 simulations with varying global mean surface air temperatures T_G: $T_G = 270$ (dotted line), 288 (blue solid line), 300 (dashed line), 311 K (dashed–dotted line). The red solid line shows the zonal mean cyclone frequency from ERA-Interim data averaged over both hemispheres.

in some other simulations with aquaplanet and full GCMs (Yin 2005; Bengtsson et al. 2006; Lu et al. 2010), and we focus here on the overall changes in cyclone statistics rather than their meridional distribution.

b. Number and intensity

We now focus on the variation of different characteristics of extratropical cyclones (with an SLP minimum along the track between 30° and 80° latitude) with global mean temperature as shown in Fig. 4. The number of extratropical cyclones (counting each track only once; Fig. 4a) is largest for the reference simulation and decreases for colder and warmer climates. Figures 4b and 4c show two measures of cyclone intensity: the minimum SLP and the lower-tropospheric relative vorticity at the time and location of minimum SLP. For comparison, the extratropical mean column-integrated EKE (not specifically sampled in cyclone areas) (see again O'Gorman and Schneider 2008a) is shown in Fig. 4d. The minimum SLP (Fig. 4b) does not vary very strongly with T_G; the median over all extratropical cyclones is only 12 hPa (9 hPa) larger in the warmest (coldest) climate than in the simulations with $T_G = 294$ K. These changes in the median are much smaller than the variations between individual cyclones in a given climate, as indicated by the percentiles (gray shading). Very similar results are obtained if the anomaly of SLP with respect to the extratropical average SLP is considered rather than the absolute value (not shown). In good correspondence to these variations of minimum SLP, the median lower-tropospheric relative vorticity associated with extratropical cyclones (Fig. 4c) peaks in the simulation with $T_G = 294$ K and is smaller in cold and warm climates. The median vorticity varies by almost a factor of 2 between the simulations with the highest and lowest median vorticity. An interesting observation is that while the median of the vorticity decreases with the global mean temperature for $T_G > 294$ K, the 95th percentile stays relatively high up to $T_G = 311$ K, indicating that the intensity of the strongest storms responds differently to climate warming than the intensity of moderately intense cyclones. This is discussed in more detail in section 4. While the SLP values associated with extratropical cyclones do not change substantially with horizontal model resolution (not shown), lower-tropospheric vorticity is much larger in the simulations with higher resolution (Fig. 5). For the reference climate, the median lower-tropospheric vorticity in the T170 simulation is increased by a factor of 3 compared to the simulation with T42 resolution. This shows that relative vorticity, in contrast to SLP, often has substantial gradients close to a cyclone center, which can only be properly resolved with relatively high model resolution. Nevertheless, all simulations show the same vorticity trend with global mean temperature as described above (highest values in the simulations slightly warmer than present day, lower vorticity for very warm and cold climates). The combined behavior of cyclone numbers and the intensity in the different

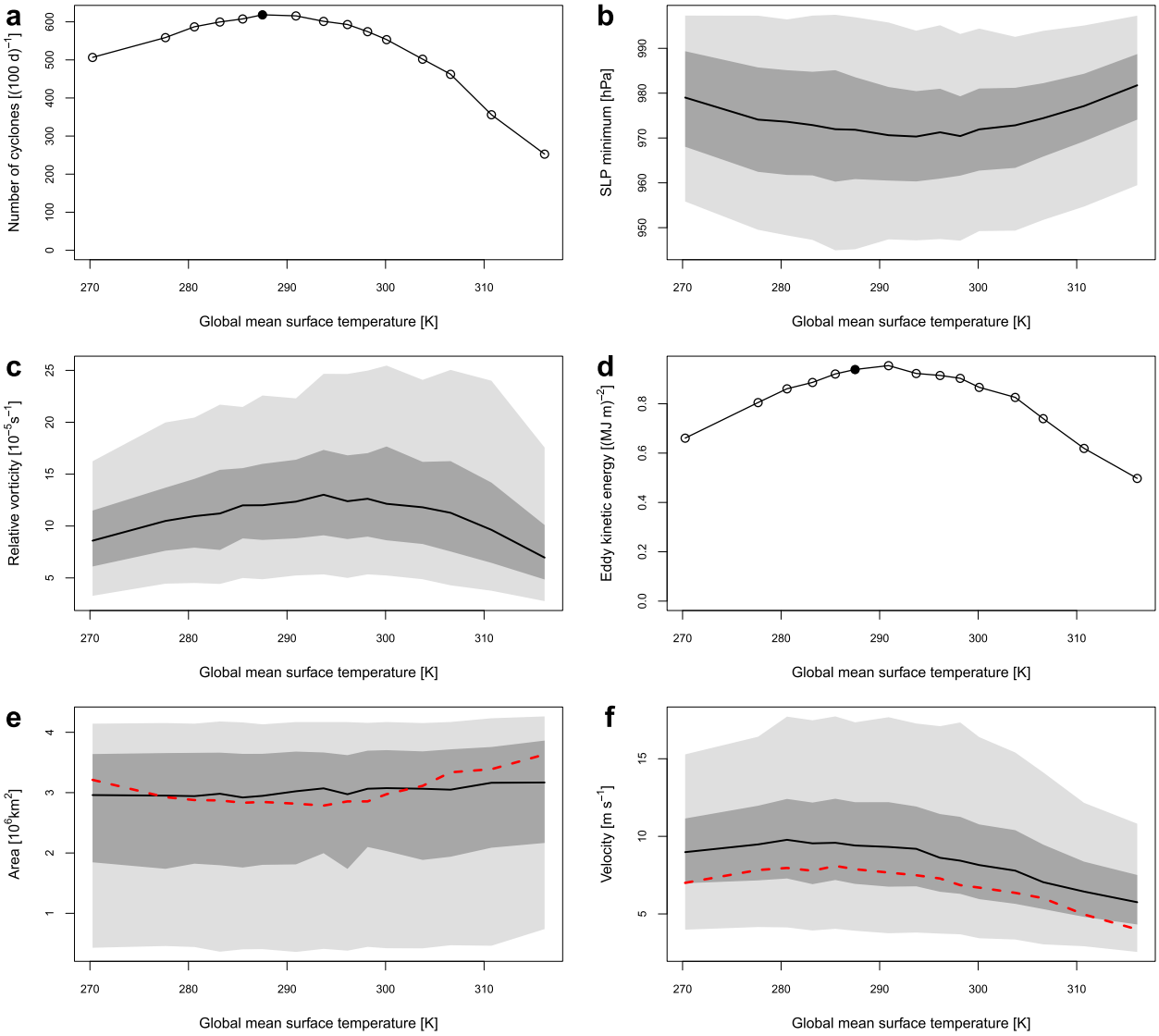

FIG. 4. Extratropical cyclone characteristics in T85 simulations as functions of the global mean surface air temperature: (a) cyclone number (counting each track only once) and the filled circle indicates the reference simulation, here and in subsequent figures; (b) minimum sea level pressure; (c) lower-tropospheric relative vorticity (at 850 hPa) at the time and location of minimum SLP, (d) climatological, column-integrated eddy kinetic energy, averaged between 30° and 80° latitude; (e) maximum cyclone size and the red dashed line shows the squared eddy length (following O'Gorman 2011), rescaled by a constant factor of 0.11, which has been determined with a least squares fit to a linear relation with the median cyclone size; and (f) average displacement velocity of the SLP minimum along cyclone tracks and the red dashed line shows the mean zonal wind speed, averaged between 30° and 80° latitude, halfway in pressure between the 2-PVU tropopause and the surface. The black lines in (b),(c),(e), and (f) show the medians over all extratropical cyclones (with SLP minimum between 30° and 80° latitude), shaded areas correspond to the upper and lower quartiles (dark gray) and the 5th and 95th percentiles (light gray).

T85 simulations (Figs. 4a–c) corresponds relatively well with changes in extratropical average EKE (Fig. 4d). All measures indicate a decrease of storminess for very cold and very warm climates. While the EKE peaks in the simulations slightly warmer than present day, the cyclone intensity maxima occur at somewhat higher temperatures. As already shown by O'Gorman and Schneider (2008a) and O'Gorman (2011), EKE in the idealized GCM simulations scales with the mean available potential energy. Factors such as cyclone lifetime may also affect EKE, but to the extent that the cyclone intensity behaves like EKE, the general trend of median cyclone intensity is thus related to changes in available energy. Therefore, the factors affecting available energy such as a decreasing low-level meridional temperature gradient, an increasing temperature gradient in the

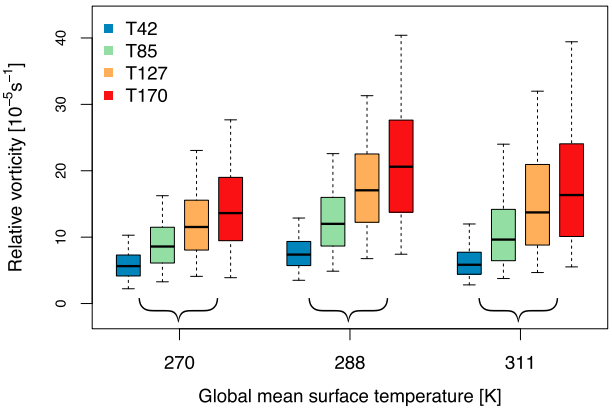

FIG. 5. Statistical distributions of the lower-tropospheric relative vorticity (at 850 hPa) at the time and location of minimum SLP of extratropical cyclones in simulations with varying global mean surface air temperatures (T_G given at the horizontal axis) and different horizontal resolutions, as shown with colors. Horizontal lines inside the boxes show the medians, boxes show the interquartile ranges, and whiskers show the 5th and 95th percentiles.

upper troposphere (cf. section 2c), an increasing tropopause height,[1] nonmonotonic changes in extratropical static stability (O'Gorman and Schneider 2008a), and increases in latent heat release (O'Gorman 2011) contribute to the changes in cyclone intensity with warming discussed above.

c. Size

The maximum cyclone size, determined as the maximum of the area within the outermost closed pressure contour along each cyclone track (cf. section 2), does not vary substantially between the different simulations (Fig. 4e). There is a small increase in the 5th percentile and lower quartile with T_G, but the median and the upper percentiles stay relatively constant. For comparison, the red dashed line in Fig. 4e shows the squared extratropical eddy length, which has been calculated from a spherical analysis of the EKE spectrum following O'Gorman (2011) and rescaled with a factor of 0.11 (determined from a least squares fit to a linear relation with the median cyclone size). This rescaling is necessary since the eddy length is largely determined by the Rossby wave pattern in the middle and upper troposphere, and the spatial scales of these Rossby waves are typically larger than the size of surface cyclones. For climates colder than the reference climate, the eddy length decreases weakly with warming. For higher global mean temperatures there is an increase of the eddy length that is more comparable to the increases in the lower percentiles of the cyclone area. A moderate increase of the eddy length with warming has also been found in other idealized models (Caballero and Hanley 2012) and in full GCM simulations of future climate (Kidston et al. 2010). O'Gorman (2011) showed that the eddy length in the idealized simulations scales with an effective Rossby radius that takes the effect of latent heat release on the static stability into account (and not with the classical dry Rossby radius). Based on this scaling, the rather small changes of eddy length with T_G are thought to relate to both the increasing depth of the troposphere and the first decreasing and then relatively constant effective static stability. Nevertheless, both the eddy length and cyclone size change only weakly over the full range of climates.

d. Translation velocity

The translation velocity of cyclones is potentially an important factor in determining the impacts of heavy precipitation and wind events. As shown in Fig. 4f, the average displacement velocity of the pressure minimum along the cyclone track (defined as the mean over the 6-hourly displacement velocities) is largest in climates slightly colder than present-day and decreases with increasing T_G for warmer climates. Caballero and Hanley (2012) also found the eddy phase speed to be decreasing with warming in aquaplanet simulations with global mean temperatures higher than present day. Since the cyclones' meridional displacement is typically small compared to their zonal movement, this behavior of the translation velocity can be related to the extratropical mean zonal wind speed. As shown by the red line in Fig. 4f, the mean zonal wind velocity in the mid troposphere, halfway in pressure between the tropopause and the surface (with the tropopause defined as the 2-PVU isoline, and PVU denotes the potential vorticity unit, $1\ \mathrm{PVU} = 10^{-6}\,\mathrm{K\,kg^{-1}\,m^2\,s^{-1}}$) follows the same tendency with T_G as the translation velocity of cyclones. Also, the absolute values of the midtropospheric zonal wind speed are similar to, albeit slightly lower than the median translation velocity, indicating that this level is close to the average steering level of the cyclones. Graff and LaCasce (2014) found a similar correspondence between zonal wind speed and zonal cyclone displacement in a more comprehensive GCM. Based on the thermal wind relation, two competing factors lead to the nonmonotonic change of the extratropical, midtropospheric zonal wind speed with T_G in our simulations; while the depth of the extratropical tropopause increases, horizontal temperature gradients (both at the surface and vertically averaged) decrease monotonically with

[1] The increase in tropopause height is linked to the increase in surface temperature through a radiative constraint (Schneider 2007), with additional influences from changes in tropospheric lapse rates and the longwave absorber.

warming (see again section 2c and O'Gorman and Schneider 2008a).

e. Deepening rates

Figure 6a shows statistics of the maximum 24-h deepening rates, calculated as the largest 24-h decrease of the minimum sea level pressure along each cyclone track. Median deepening rates are on the order of 5–6 hPa day^{-1}. They are relatively constant over a wide range of climates and decrease only for very warm climates. The upper quartile and particularly the 95th percentile are more variable, with the 95th percentile peaking at 20 hPa day^{-1} for $T_G = 294$ K. Similar results are obtained for deepening rates in units of Bergeron (i.e., the equivalent pressure tendency at 60° latitude; Sanders and Gyakum 1980) (not shown). This finding of maximum deepening rates in climates slightly warmer than present day is consistent with the other measures of cyclone intensity discussed above (see again Figs. 4b–d). The smaller deepening rates in warmer and (to some degree) colder climates are also associated with longer cyclone lifetimes (Fig. 6c), especially with respect to the upper percentiles.

To compare the empirical deepening rates with theoretical predictions, the maximum 24-h deepening rates are normalized with the SLP anomaly at the beginning of the 24-h deepening period. These SLP anomalies are calculated with respect to the zonal- and time-mean SLP, and only cyclones with anomalies of more than 1 hPa are taken into account. The median of the normalized deepening rates increases just slightly over the different simulations, whereas the upper quartile and 95th percentile are larger in warmer climates, with maxima between $T_G = 298$ and 311 K (Fig. 6b). To better understand how these deepening rates relate to changes in the atmospheric mean state, maximum linear growth rates of baroclinic instability under the quasigeostrophic approximation are calculated numerically following the approach of Smith (2007). Vertical profiles of zonal wind and thermal stratification from the simulations, calculated as time, zonal, and area-weighted meridional means over the midlatitude baroclinic zones in both hemispheres, are used as the base state. Following O'Gorman and Schneider (2008a), the baroclinic zones are defined as the regions within 15° latitude of the maximum of the vertically integrated eddy potential temperature flux. The parameters f and β are also set based on this latitude (note that the linear growth rates do not correctly capture the location of the storm track if calculated for different latitude bands). Either the dry stratification is used or the effective static stability of O'Gorman (2011) is used above 900 hPa to account for latent heat release; this effective static stability has previously been shown

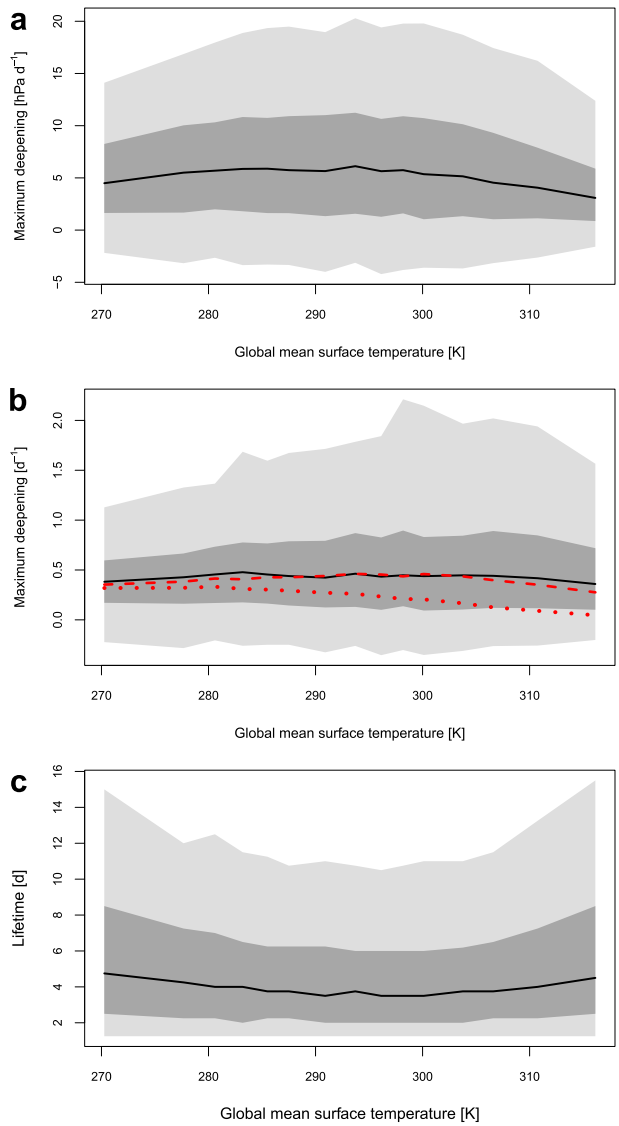

FIG. 6. Further extratropical cyclone characteristics in T85 simulations as functions of the global mean surface air temperature. (a) Maximum daily deepening rate (most pronounced SLP decrease) along the cyclone track. (b) Maximum daily deepening rate, normalized with the SLP anomaly relative to the zonal-mean climatology. Only cyclones with SLP anomalies of more than 1 hPa are taken into account. The red dotted line shows quasigeostrophic linear growth rates for a dry atmosphere, and the red dashed line shows growth rates calculated with the effective static stability of O'Gorman (2011). (c) Lifetime of cyclones. Black lines and shading as in Fig. 4.

to capture the effect of latent heating on growth rates in baroclinic life cycles provided the initial relative humidity is sufficiently high (Booth et al. 2015). The height coordinate of Smith (2007) is replaced by a pressure coordinate for application to the atmosphere rather than ocean, and the equations are modified so that the bottom boundary condition remains as $w = 0$, where w is the

vertical velocity in height coordinates. Rayleigh damping of relative vorticity is imposed below 850 hPa as an idealized representation of boundary layer drag, with the Rayleigh damping coefficient set to $2\,\mathrm{day}^{-1}$ at the surface and decreasing linearly in pressure to a value of zero at 850 hPa (cf. Merlis and Schneider 2009). Using Ekman pumping at the surface rather than Rayleigh damping in the interior gives similar results and is dynamically more consistent given that the calculation neglects ageostrophic advection, but we chose to use Rayleigh damping because it better represents the finite depth of the boundary layer in the GCM simulations. The meridional wavenumber is set to zero in all cases. The resulting maximum linear growth rates are shown as red lines in Fig. 6b. Both linear growth rates calculated with dry and effective static stability are close to the median empirical deepening rate for very cold climates. However, the dry linear growth rate decreases with increasing T_G, whereas the effective growth rate stays relatively constant, in good quantitative agreement with the median deepening rate. Taking the effect of latent heat release on the vertical stratification into account is thus essential for capturing this behavior of the cyclone deepening rates. It should be emphasized here that the calculated linear growth rates refer to the most unstable normal modes of the quasigeostrophic system, whereas deepening rates are diagnosed for cyclones, which may experience transient growth that is faster than the growth of the most unstable normal mode (Farrell 1982). Badger and Hoskins (2001) considered a simple nonmodal initial value problem and found that the maximum growth rate was equal to the maximum normal-mode growth rate (as given by the Eady growth rate) multiplied by a constant greater than one. Therefore, although we only calculate normal-mode growth rates, the nonmodal growth rates may also scale in a similar way across climates (even if their magnitudes are greater). However, the scaling of the 95th percentile of the normalized deepening rates with T_G is noticeably different from that of the median normalized deepening rates and the linear growth rates (see again Fig. 6b). One possible explanation for this different scaling is that the mean effective static stability is adequate to represent the reduction in static stability from latent heating for cyclones with typical normalized deepening rates, but not for the most explosive cyclones.

f. Skewness of deepening rates

Moisture, through latent heat release, is thought to have an asymmetrical effect on pressure changes along cyclone tracks; cyclone deepening is associated with upward vertical motion, and, according to the quasigeostrophic omega equation, latent heating preferentially strengthens upward motion by effectively reducing the static stability when there is saturated ascent. Because of this asymmetry, the positive skewness found in statistical distributions of cyclone deepening has been attributed to latent heating (Roebber 1984; Roebber and Schumann 2011). Here we investigate how this skewness changes with changing climate. In contrast to Roebber (1984) and Roebber and Schumann (2011), we do not only use the maximum daily pressure decrease, but all 6-hourly (positive and negative) pressure changes along all extratropical cyclone tracks in each simulation to estimate statistical deepening distributions (the reason for this change in approach is that taking the maximum of the pressure decreases does not preserve the characteristics of the statistical distribution and can lead to skewness by itself). Figure 7a shows the estimated deepening distributions from four of the simulations that span a wide range of climates. Consistent with the daily maximum deepening shown in Fig. 6a, the distributions from simulations with intermediate temperatures have longer tails compared to the very cold and very warm simulations, indicating stronger deepening and filling of cyclones. Horizontal model resolution only moderately affects these distributions (Fig. 7b). Note, however, that the deepening distribution of oceanic cyclones from the ERA-Interim dataset (red line in Fig. 7b) is substantially broader. This may partly be due to the increased baroclinicity in specific regions in the reanalysis data (e.g., downstream of the continents), but may also indicate problems of the idealized GCM with fully capturing explosive cyclone development. As evident from Fig. 7a, the deepening distributions are skewed toward positive values (i.e., stronger deepening than filling). This is quantified by calculating the skewness (the standardized third moment) of each distribution (cf. Roebber and Schumann 2011). The skewness is higher for warm than for cold climates, varying between roughly 0.5 and 0.9 across the T85 simulations, with a relatively abrupt transition between $T_G = 296$ and 298 K (Fig. 8a). This is consistent with the increased atmospheric moisture content and thus larger potential contribution of latent heating to cyclone intensification in these warmer climates. Although there is some variability in the skewness from similar climates and from simulations with different horizontal resolution (different symbols in Fig. 8a), the overall increase with T_G is much larger than the estimated sampling error (red error bar in Fig. 8a). The skewness also increases with warming when it is calculated based on pressure anomalies with respect to the zonal mean rather than absolute pressure values, and in this case the rate of increase is steadier over the full range of climates (not shown). The skewness obtained

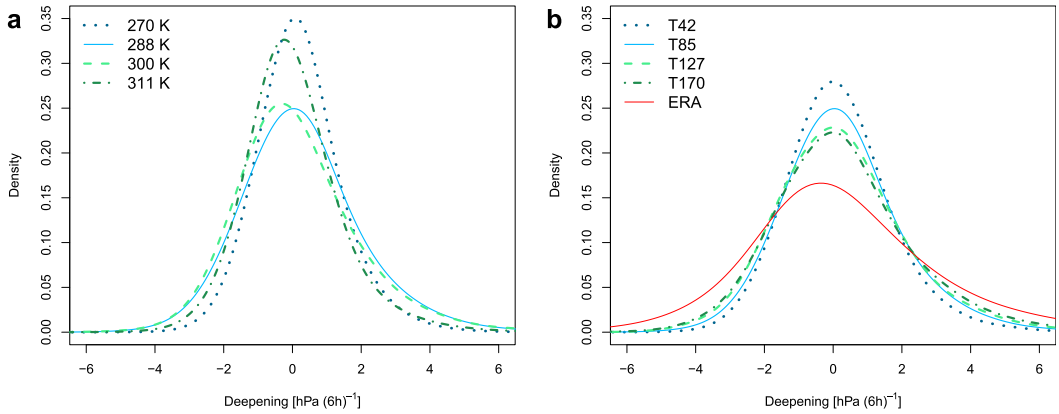

FIG. 7. Probability density functions (PDFs) of 6-hourly deepening (positive values refer to SLP decrease) along extratropical cyclone tracks in (a) T85 simulations with varying global mean surface air temperatures and (b) simulations with different horizontal resolutions and T_G = 288 K. PDFs have been estimated with a nonparametric fit using Gaussian kernels and taking all 6-hourly time steps from all cyclones into account. The red line in (b) shows the same PDF based on ERA-Interim data, using only cyclone locations over the ocean.

from the reference simulation (filled symbol in Fig. 8a) agrees well with the skewness of oceanic cyclones in ERA-Interim (Fig. 8b). For cyclones over land, where the moisture availability is limited, the skewness is greatly reduced, and even becomes negative in Southern Hemisphere winter. Maximum skewness over land is found in Northern Hemisphere summer. These land–ocean differences are probably not only due to differences in the moisture availability, but may also relate to the larger surface friction over land, which leads to more rapid cyclone decay, and the geographical positions of the starts and ends of the storm tracks. In summary, these results are consistent with previous findings relating the skewness of cyclone deepening distributions to moist processes and latent heat release. In addition, they indicate that these processes may lead to increased skewness as the climate warms.

4. Analysis of intense cyclones

To obtain a more detailed picture of changes in cyclone characteristics with climate, composite fields centered on intense extratropical cyclones are analyzed. The selection of intense cyclones is described in detail in section 2b; they correspond to the most intense 10% of cyclones for the reference simulation. Figure 9 shows the composite SLP and relative vorticity at 850 hPa from four representative simulations: a very cold one, the reference simulation, a warm simulation, and a very warm simulation. The corresponding lower-tropospheric temperature anomaly composites are

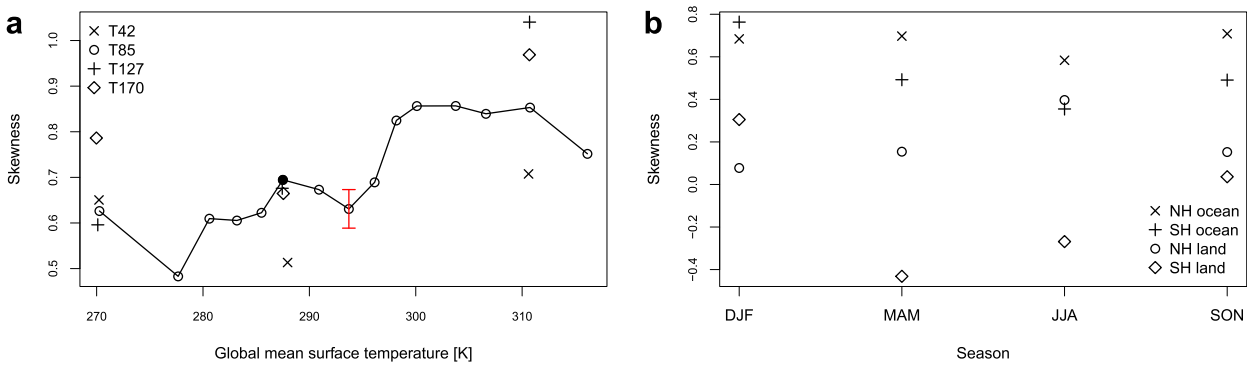

FIG. 8. (a) Skewness of cyclone deepening distributions from simulations with varying global mean surface air temperatures (given on the horizontal axis) and different horizontal resolutions (different symbols). The sampling error is illustrated by the red error bar shown for the simulation with T_G = 294 K, which represents a 90% confidence interval estimated using a bootstrapping approach. (b) Skewness of cyclone deepening distributions from ERA-Interim data shown for different seasons by hemispheric land and ocean grid points (symbols).

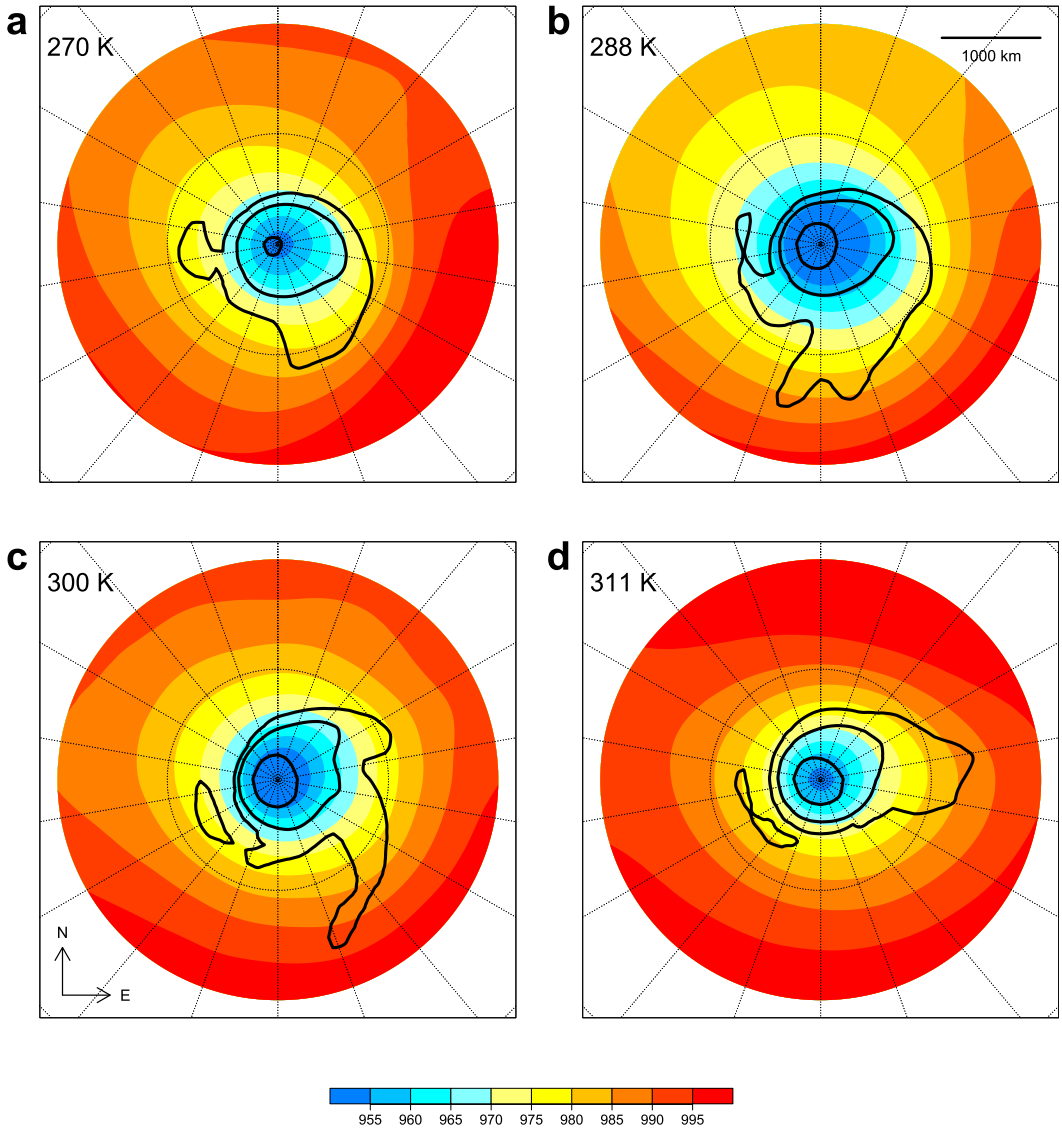

FIG. 9. Composite sea level pressure (color shading; hPa) and lower-tropospheric relative vorticity (at 850 hPa; black contours of 1, 3, and $12 \times 10^{-5}\,\mathrm{s}^{-1}$) of intense extratropical cyclones (defined in section 2b) at the time of SLP minimum in T85 simulations with varying global mean surface air temperatures: T_G = (a) 270, (b) 288, (c) 300, and (d) 311 K.

shown in Fig. 10. The structure of intense cyclones in terms of SLP and relative vorticity is similar in the different climates. Minor differences are that the SLP minimum is slightly lower in the simulations with T_G = 288 and 300 K compared to the very cold and very warm climates, consistent with the statistical results presented in section 3. The large-scale SLP gradient is stronger in the equatorward than in the poleward direction in the colder climates (Figs. 9a and 9b), while the SLP structure is rather symmetric in the very warm climate (Fig. 9d). Consistent with these SLP patterns, enhanced relative vorticity values (and thus near-surface wind maxima) extend more in the equatorward direction (within the warm sector, ahead of the cold front, cf. Fig. 10) in the colder simulations, but are found mostly around and eastward of the cyclone center (in the region of the warm front) in the very warm run. In contrast to these relatively small changes in SLP and vorticity, the 850-hPa temperature anomaly structure differs a lot between cold and warm climates (Fig. 10). The large-scale horizontal temperature gradient as well as the gradients at the warm and cold fronts decrease strongly with increasing global mean temperature. This is consistent with the generally reduced lower-tropospheric meridional temperature gradient in the warmer simulations (see again section 2c). Similar to the horizontal

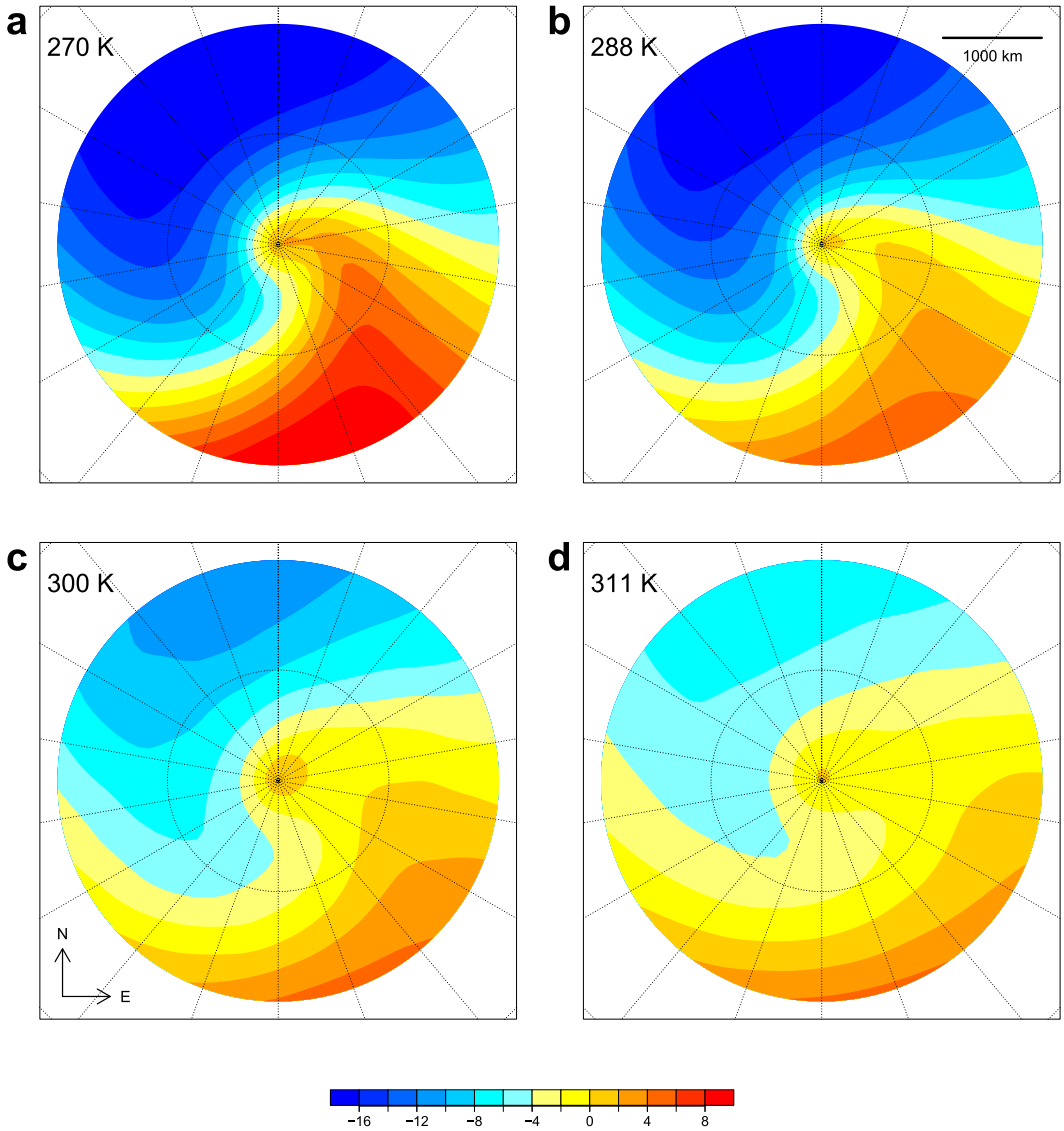

FIG. 10. Composite lower-tropospheric temperature anomaly with respect to the mean extratropical temperature (at 850 hPa; K) associated with intense extratropical cyclones at the time of SLP minimum in T85 simulations with varying global mean surface air temperatures: T_G = (a) 270, (b) 288, (c) 300, and (d) 311 K.

temperature structure, vertical temperature gradients associated with extratropical cyclones also vary substantially between the different simulations (Fig. 11). The vertical potential temperature (θ) gradients within cyclones are found to be lowest in the reference simulation and in colder climates (Fig. 11a). In the very cold simulation, the stratification is somewhat more stable. The vertical θ gradient increases monotonically with T_G in the simulations warmer than present-day Earth. In the warmest simulation, the vertical θ gradient is almost twice as large as in the reference run. This increase of dry stability within cyclones is again consistent with the general trend of the extratropical stratification in the idealized model (O'Gorman and Schneider 2008a). The changes in extratropical dry static stability have been shown to be related to a roughly constant supercriticality for moist baroclinic eddies (O'Gorman 2011), except in the warmest climates in which the stratification becomes moist adiabatic (Fig. 11b). Note, however, that the effective static stability experienced by cyclones is a combination of dry and moist static stabilities and does not vanish even for a moist adiabatic stratification (O'Gorman 2011). The differences in vertical stratification between simulations with varying horizontal resolutions (different symbols in Fig. 11) are relatively minor, but interestingly they are larger in the cold than

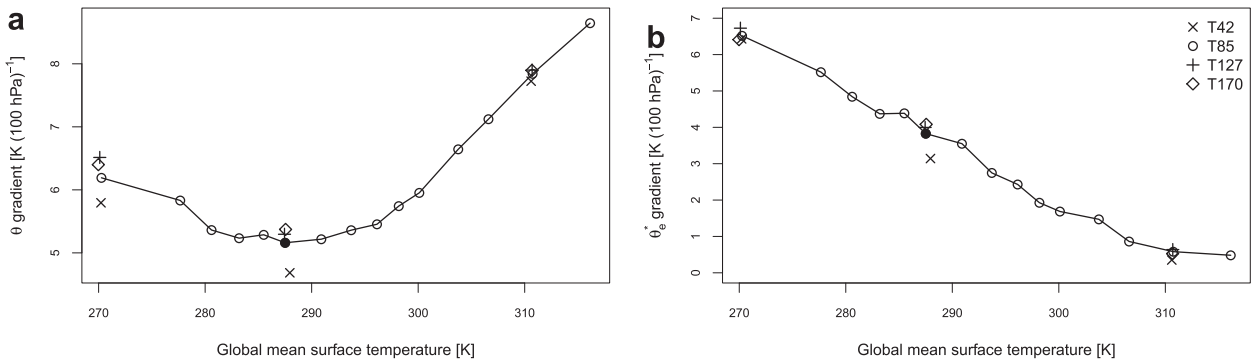

FIG. 11. Mean vertical potential temperature gradients associated with intense extratropical cyclones as functions of the global mean surface air temperature. (a) Gradient of potential temperature, calculated from the difference between θ at 500 and 900 hPa (averaged in a radius of 350 km around the cyclone center). (b) Gradient of saturated equivalent potential temperature θ_e^*, calculated from the difference between θ_e^* at 500 and 700 hPa. Simulations with varying horizontal resolutions are shown with different symbols.

in the warm simulations. The moist adiabatic stratification approached in the warm climates appears to be a strong constraint independent of the model resolution.

The composite precipitation associated with intense extratropical cyclones increases strongly with T_G (Fig. 12), in line with the general trend of total and extreme precipitation in the idealized simulations (O'Gorman and Schneider 2008b, 2009) and cyclone-related precipitation in comprehensive GCM simulations of future climate (Zappa et al. 2013). In the very cold simulation, a substantial part of the precipitation falls in the warm sector, far away from the SLP minimum (Fig. 12a). With increasing global mean temperature, more precipitation is found at the warm front and near the center of the cyclone, with the maximum to its west. This shift in the spatial patterns is linked to the much larger horizontal temperature gradient in the colder climates (see again Fig. 10), which goes along with a large gradient also in the atmospheric moisture content. That is, for low T_G much more moisture is available farther equatorward of the cyclone center compared to the more poleward regions, whereas in warmer climates the percentage differences in specific humidity between high and low latitudes are smaller and the precipitation maxima occur in the region of the strongest updrafts, typically close to the SLP minimum. The generally increasing trend of precipitation with T_G levels off for very warm climates, and the area-averaged precipitation (in a radius of 1000 km around the cyclone center) even decreases between $T_G = 311$ and 316 K (not shown). Here the increasing moisture content is overcompensated by a strong decrease of the updraft velocity.

A dynamical perspective on the structure of extratropical cyclones can be obtained by looking at associated potential vorticity anomalies (e.g., Hoskins et al. 1985; Reed et al. 1992; Stoelinga 1996; Campa and Wernli 2012). Vertical PV anomaly profiles for intense cyclones from four simulations are shown in Fig. 13. In the reference simulation (Fig. 13b), two distinct PV anomalies in the upper and lower troposphere can be identified. The upper anomaly above 500 hPa is a signature of an upper-level wave and associated with a lowering of the dynamical tropopause (red lines in Fig. 13). The anomaly in the lower troposphere, with a maximum slightly above 900 hPa, most probably is produced by diabatic processes, mostly by the latent heating during cloud formation, as shown in various case studies (Reed et al. 1992; Davis 1992; Davis et al. 1993; Stoelinga 1996; Lackmann 2002; Ahmadi-Givi et al. 2004). While typically these two anomalies are displaced in the horizontal during cyclone intensification, with the upper anomaly farther to the west (Hoskins et al. 1985), they often align at the time of highest intensity to form a so-called PV tower (Reed et al. 1992; Rossa et al. 2000). The PV anomaly profiles from the reference simulation are similar to those found by Campa and Wernli (2012) based on reanalysis data (see their Fig. 3a), in particular with respect to the structure in the lower and middle troposphere. The upper-tropospheric anomaly in the idealized model is weaker, which may be due to methodological differences (with respect to cyclone sampling and the averaging radius, cf. section 2) or the idealized nature of the model. The PV anomaly profiles from the four simulations differ in several respects (see again Fig. 13); the lower-tropospheric anomaly is stronger and located at higher altitudes in the warmer climates, indicating an increase also in the altitude of maximum diabatic heating. The PV anomaly minimum in the middle troposphere occurring in the colder simulations (around 600 hPa in the reference run) vanishes in the warmer climates, and for $T_G = 311$ K a continuous anomaly of around 1 PVU in the median is found between 800 and 400 hPa. In this case the PV tower

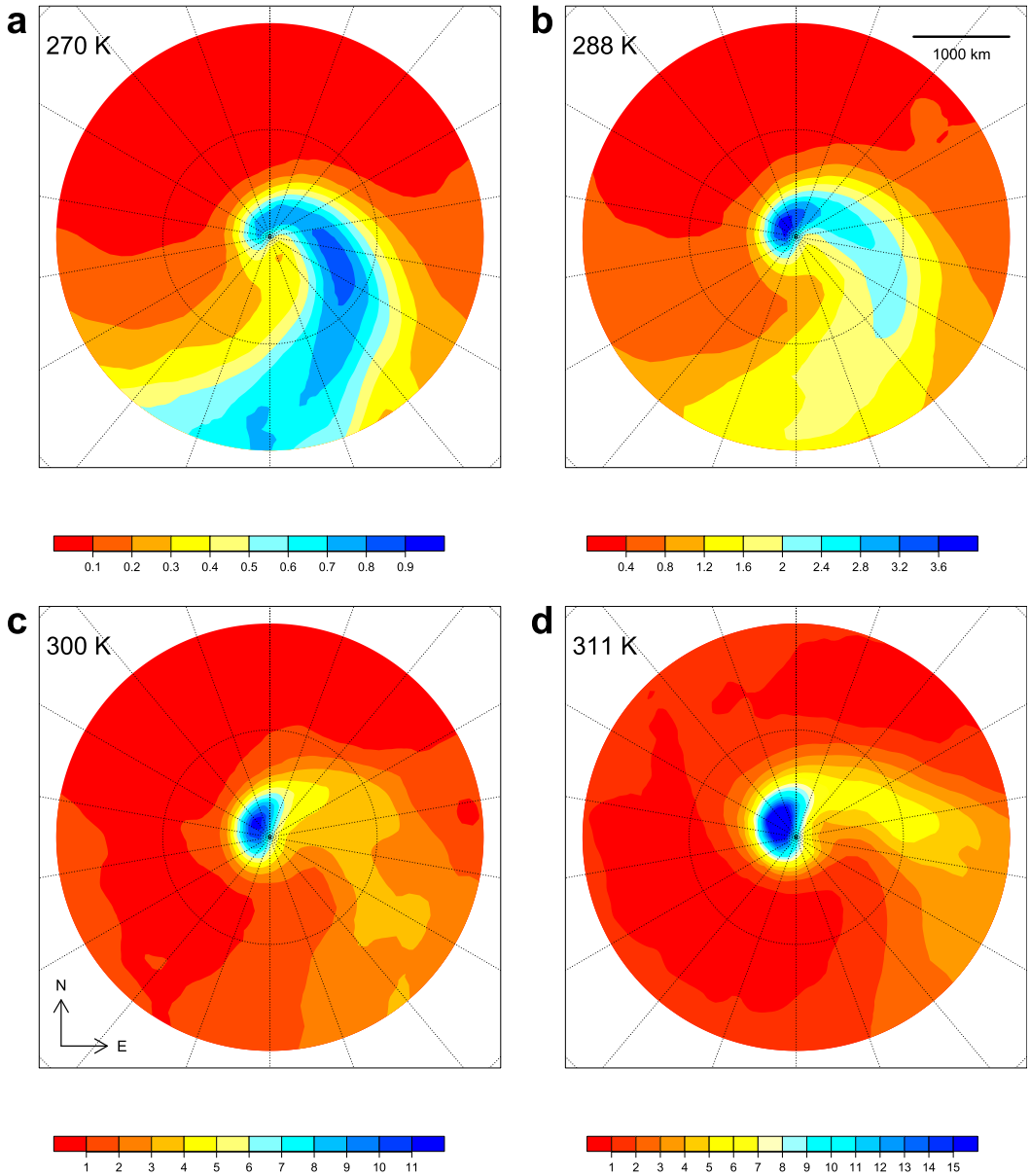

FIG. 12. Composite surface precipitation [mm (6 h)$^{-1}$] associated with intense extratropical cyclones at the time of SLP minimum in T85 simulations with varying global mean surface air temperatures: T_G = (a) 270, (b) 288, (c) 300, and (d) 311 K. Note the different color bars for each panel.

structure is very pronounced. The lowering of the tropopause is less distinct in the run with T_G = 300 K compared to the colder simulations. Note that in the very warm simulation the 2-PVU surface is not a good measure of the tropopause height in the presence of cyclones, as PV values are more elevated also at lower levels. Using a higher PV value yields more consistent results (i.e., a relatively small lowering of the tropopause in the presence of cyclones; not shown). Median PV anomalies associated with moderate cyclones (blue lines in Fig. 13) are consistently less pronounced compared to the intense cyclones, which is again in agreement with the results of Campa and Wernli (2012) for the present-day climate. The difference is larger in warm than in cold climates; for T_G = 311 K, the median anomalies of moderate cyclones are smaller than the 5th percentiles from intense cyclones throughout most of the troposphere.

A more concise picture of the evolution of the cyclones' PV structure is obtained by calculating vertically averaged anomalies in the upper troposphere (UT; averaged from 100 hPa below to the level of the

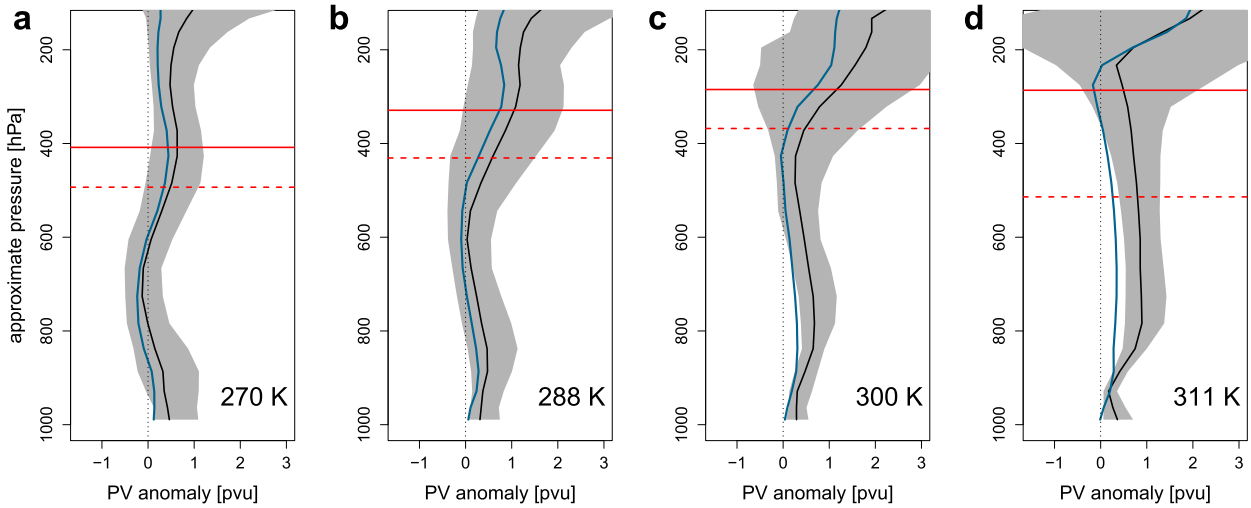

FIG. 13. Vertical profiles of potential vorticity anomalies associated with intense extratropical cyclones at the time of SLP minimum in T85 simulations with varying global mean surface air temperatures: T_G = (a) 270, (b) 288, (c) 300, and (d) 311 K. Anomalies are calculated with respect to a local PV climatology and averaged in a radius of 350 km around the cyclone center. Black lines show the medians, and gray shading shows the 5th and 95th percentiles. The red solid lines show the climatological height of the extratropical 2-PVU tropopause, and the red dashed lines indicate the 2-PVU tropopause in the presence of cyclones. Medians of PV anomaly profiles from moderate cyclones are shown with blue lines.

climatological 2-PVU tropopause) and lower troposphere (LT; 950–600 hPa), as shown in Figs. 14a and 14b, respectively. Mean UT anomalies are largest in the simulations with T_G between 291 and 300 K and decreases in warmer climates both for intense and average cyclones. In contrast to that, the LT PV anomaly of intense cyclones increases monotonically with T_G up to the second-to-warmest simulation (Fig. 14b). This indicates that diabatic PV production through latent heating becomes more and more important as climate warms, in line with the increasing atmospheric moisture content and average precipitation in the cyclone area. In fact, also the leveling off and final decrease of the mean LT PV anomaly in very warm climates is very similar to the precipitation trend, and the correlation between the two parameters is almost perfect (r = 0.99). Note that similar enhancements of lower-tropospheric PV anomalies in a warmer climate have been found for tropical cyclones (Hill and Lackmann 2011) and intense U.S. East Coast cyclones in a regional model study (Marciano et al. 2015). For moderate cyclones (blue line in Fig. 14b), the rate of increase of the LT PV anomaly with T_G is lower than for intense cyclones. Note that the magnitudes of both UT and LT PV anomalies depend on the model resolution (see the different symbols in Fig. 14) and are much lower in the coarse T42 simulations.

As already noted in section 3, the intensity of strong cyclones behaves differently under changing climate compared to the intensity of moderate cyclones (see again Fig. 4c). This is also evident from the mean lower-tropospheric relative vorticity (averaged in a radius of 350 km around the cyclone center) associated with the cyclones analyzed in this section, as shown in Fig. 14c. In contrast to the moderate cyclone intensity and EKE, the mean vorticity of intense cyclones does not peak in climates similar to or slightly warmer than the reference climate, but increases with T_G also for warmer climates. This increase most probably is associated with compensating effects between a reduced baroclinicity (see section 2c) and enhanced latent heat release manifested in increasing lower-tropospheric PV production. MAPE (and hence EKE) is also affected by changes in baroclinicity and the increases in latent heat release (O'Gorman 2011), but the increases in latent heat release seem to have less of an effect on the scaling of MAPE than on the scaling of the relative vorticity in the intense cyclones. In contrast to the intense cyclones, the PV production associated with moderate cyclones is less pronounced, leading to a reduction of lower-tropospheric vorticity and thus a wider range of cyclone intensities in warmer climates. While the mean vorticity from the higher-resolution simulations is similar to the T85 resolution results, the values from the coarse-resolution T42 runs are substantially lower (see again Fig. 14c). In particular, the increasing trend of the vorticity of intense cyclones from the reference to the very warm simulation is not captured with low resolution, probably indicating problems with resolving diabatic processes. Further differences can be expected

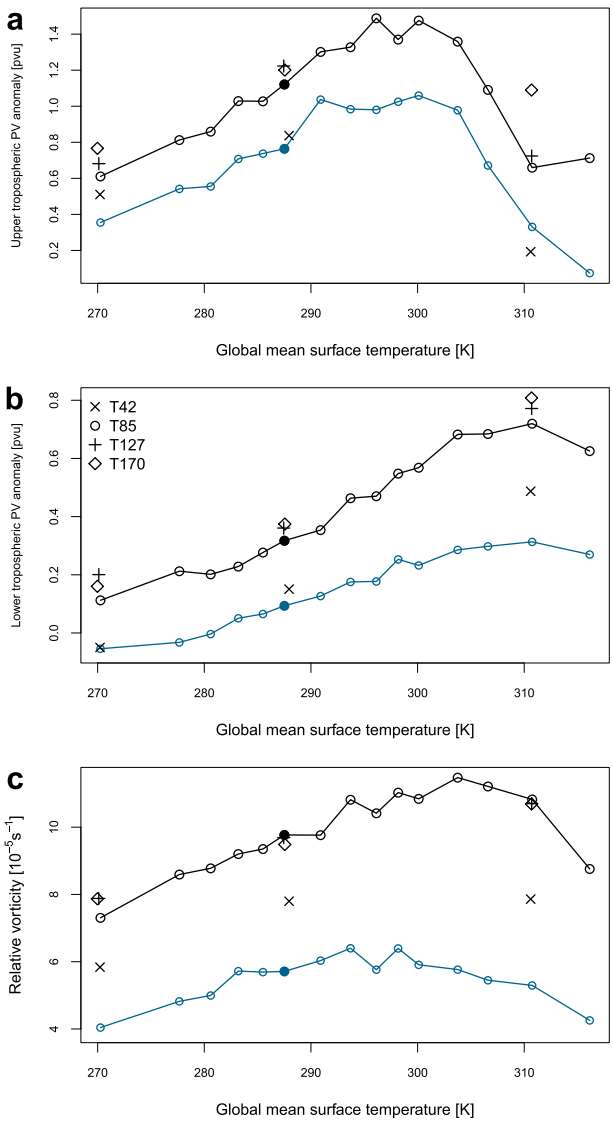

FIG. 14. Mean horizontally averaged PV and relative vorticity (in a radius of 350 km around the cyclone center) associated with intense extratropical cyclones in simulations with varying global mean surface air temperatures (given at the horizontal axes) and different horizontal resolutions (different symbols): (a) upper-tropospheric PV anomaly (averaged from 100 hPa below to the level of the climatological 2-PVU tropopause), (b) lower-tropospheric PV anomaly (averaged between 950 and 600 hPa), and (c) lower-tropospheric relative vorticity (at 850 hPa). The blue lines show mean PV and vorticity of moderate cyclones.

when the resolution is increased beyond the values used in this study (Willison et al. 2013).

5. Conclusions

Idealized GCM simulations have been used in this study together with a cyclone tracking scheme to investigate changes in the characteristics of extratropical cyclones in different climates. In spite of huge variations in the global mean near-surface temperature between the different simulations, the structure of extratropical cyclones in terms of sea level pressure and vorticity is relatively similar. Also the size of the cyclones changes only marginally with T_G, in broad agreement with variations in eddy length and effective Rossby radius. Cyclone translation velocities peak in climates slightly colder than present day and scale with the mean zonal wind speed in the free troposphere. Changes in deepening rates are also relatively small, which is shown to be consistent with linear, quasigeostrophic growth rates based on the mean state when latent heating is accounted for using an effective static stability. We use growth rates of normal modes for the comparison, but the results of Badger and Hoskins (2001) suggest that nonmodal growth rates may scale similarly. The median cyclone intensity is largest in simulations with T_G around 294 K, roughly consistent with the variation of extratropical mean eddy kinetic energy. This nonmonotonic trend is associated with partly compensating changes in mean horizontal temperature gradients, vertical stability, and the depth of the troposphere. However, for very intense cyclones the lower-tropospheric vorticity does not follow the same trend as the median intensity, but peaks in considerably warmer climates. Similarly, the 95th percentile of the normalized deepening rates continues to increase with warming up to the warmest climates, and the skewness of the deepening rates increases as the climate warms.

Most studies based on future climate scenarios or experiments with increased atmospheric CO_2 content have found only minor changes in cyclone intensity measured in terms of vorticity or wind speed (Bengtsson et al. 2009; Catto et al. 2011; Zappa et al. 2013), and there are substantial regional variations as well as uncertainties evident from intermodel differences (Zappa et al. 2013; Colle et al. 2013). Similar results have been obtained in other recent studies using an analog approach (Li et al. 2014) or idealized baroclinic channel simulations (Booth et al. 2013). This is consistent with our findings, which also imply minor cyclone intensity variations for a comparably small range of temperature changes. The advantage of our idealized investigation is that relatively large signals can be produced by strongly varying the climate conditions, and the complexity (e.g., with respect to regional patterns) is reduced, allowing a focus on the most important physical processes. Consistent with previous studies based on EKE, we have found that changes in median cyclone intensity can to first order be explained by variations in baroclinicity and the vertical structure of the atmosphere. Nevertheless, several lines of evidence also indicate an important role

of the increased moisture content and latent heating in warmer climates; quasigeostrophic theory can only explain the changes in cyclone deepening rates if the effect of latent heat release on the stratification is taken into account. The skewness of deepening distributions increases with increasing global mean temperature. Lower-tropospheric potential vorticity anomalies are more pronounced in warmer climates, most likely due to enhanced latent heating. For intense cyclones, this strengthening of diabatic lower-tropospheric PV anomalies overcompensates for the decrease in baroclinicity, resulting in a maximum of lower-tropospheric vorticity in very warm climates. This effect of latent heating on the most intense cyclones seems to be greater than its effect on MAPE and, hence, mean EKE. Other studies based on higher-resolution regional simulations have also detected substantial effects of enhanced latent heat on the intensity of individual storms (Ludwig et al. 2014; Marciano et al. 2015).

A drawback of the idealized GCM used for the present study is that changes in the mass of the atmospheric column due to evaporation and precipitation are not taken into account. In particular in the warmer simulations, the increased mass convergence in cyclones resulting from a larger precipitation mass sink may increase vorticity and precipitation beyond what is found in the idealized GCM. This effect can be expected to be strongest in the most intense cyclones and may thus further increase the sensitivity of these intense cyclones to climate warming. This anticipated role of mass changes due to precipitation and evaporation in different climates should be examined in more detail in future research.

Moist processes are already relevant in our simulations with horizontal resolutions up to T170, and even larger effects can be expected with higher resolution when mesoscale structures like fronts are properly represented (Willison et al. 2013). Investigating such resolution effects in an idealized setup will be another focus of future research. Finally, this study shows that there is a need for developing a more comprehensive theory of the influence of moisture on extratropical storms that allows for quantitative predictions of latent heat effects not only on characteristics of moderate cyclones or EKE, but also on characteristics of intense cyclones and the tail of the distribution of deepening rates.

Acknowledgments. MeteoSwiss and ECMWF are acknowledged for giving access to the ERA-Interim dataset. We thank Michael Sprenger for technical help with the cyclone tracking as well as Lukas Papritz and Heini Wernli for helpful discussions. PAOG and MSS acknowledge support from NSF Grant AGS-1148594 and computing support from NCAR's Computational and Information Systems Laboratory (http://n2t.net/ark:/85065/d7wd3xhc). The model output and cyclone tracking data are available upon request.

REFERENCES

Ahmadi-Givi, F., G. C. Craig, and R. S. Plant, 2004: The dynamics of a midlatitude cyclone with very strong latent-heat release. *Quart. J. Roy. Meteor. Soc.*, **130**, 295–323, doi:10.1256/qj.02.226.

Arakawa, A., and M. J. Suarez, 1983: Vertical differencing of the primitive equations in sigma coordinates. *Mon. Wea. Rev.*, **111**, 34–45, doi:10.1175/1520-0493(1983)111<0034:VDOTPE>2.0.CO;2.

Badger, J., and B. J. Hoskins, 2001: Simple initial value problems and mechanisms for baroclinic growth. *J. Atmos. Sci.*, **58**, 38–49, doi:10.1175/1520-0469(2001)058<0038:SIVPAM>2.0.CO;2.

Bengtsson, L., K. I. Hodges, and E. Roeckner, 2006: Storm tracks and climate change. *J. Climate*, **19**, 3518–3543, doi:10.1175/JCLI3815.1.

——, ——, and N. Keenlyside, 2009: Will extratropical storms intensify in a warming climate? *J. Climate*, **22**, 2276–2301, doi:10.1175/2008JCLI2678.1.

Birner, T., D. W. J. Thompson, and T. G. Shepherd, 2013: Upgradient eddy fluxes of potential vorticity near the subtropical jet. *Geophys. Res. Lett.*, **40**, 5988–5993, doi:10.1002/2013GL057728.

Blackmon, M. L., J. M. Wallace, N. C. Lau, and S. L. Mullen, 1977: An observational study of the Northern Hemisphere wintertime circulation. *J. Atmos. Sci.*, **34**, 1040–1053, doi:10.1175/1520-0469(1977)034<1040:AOSOTN>2.0.CO;2.

Booth, J. F., S. Wang, and L. Polvani, 2013: Midlatitude storms in a moister world: Lessons from idealized baroclinic life cycle experiments. *Climate Dyn.*, **41**, 787–802, doi:10.1007/s00382-012-1472-3.

——, L. Polvani, P. A. O'Gorman, and S. Wang, 2015: Effective stability in a moist baroclinic wave. *Atmos. Sci. Lett.*, **16**, 56–62, doi:10.1002/asl2.520.

Boutle, I. A., S. E. Belcher, and R. S. Plant, 2011: Moisture transport in midlatitude cyclones. *Quart. J. Roy. Meteor. Soc.*, **137**, 360–373, doi:10.1002/qj.783.

Brayshaw, D. J., B. Hoskins, and M. Blackburn, 2008: The storm-track response to idealized SST perturbations in an aquaplanet GCM. *J. Atmos. Sci.*, **65**, 2842–2860, doi:10.1175/2008JAS2657.1.

Caballero, R., and P. L. Langen, 2005: The dynamic range of poleward energy transport in an atmospheric general circulation model. *Geophys. Res. Lett.*, **32**, L02705, doi:10.1029/2004GL021581.

——, and J. Hanley, 2012: Midlatitude eddies, storm-track diffusivity, and poleward moisture transport in warm climates. *J. Atmos. Sci.*, **69**, 3237–3250, doi:10.1175/JAS-D-12-035.1.

Campa, J., and H. Wernli, 2012: A PV perspective on the vertical structure of mature midlatitude cyclones in the Northern Hemisphere. *J. Atmos. Sci.*, **69**, 725–740, doi:10.1175/JAS-D-11-050.1.

Catto, J. L., L. C. Shaffrey, and K. I. Hodges, 2010: Can climate models capture the structure of extratropical cyclones? *J. Climate*, **23**, 1621–1635, doi:10.1175/2009JCLI3318.1.

——, ——, and ——, 2011: Northern Hemisphere extratropical cyclones in a warming climate in the HiGEM high-resolution

climate model. *J. Climate*, **24**, 5336–5352, doi:10.1175/2011JCLI4181.1.

Chang, E. K. M., 2013: CMIP5 projection of significant reduction in extratropical cyclone activity over North America. *J. Climate*, **26**, 9903–9922, doi:10.1175/JCLI-D-13-00209.1.

——, S. Lee, and K. L. Swanson, 2002: Storm track dynamics. *J. Climate*, **15**, 2163–2183, doi:10.1175/1520-0442(2002)015<02163:STD>2.0.CO;2.

——, Y. Guo, X. Xia, and M. Zheng, 2013: Storm-track activity in IPCC AR4/CMIP3 model simulations. *J. Climate*, **26**, 246–260, doi:10.1175/JCLI-D-11-00707.1.

Colle, B. A., Z. Zhang, K. A. Lombardo, E. Chang, P. Liu, and M. Zhang, 2013: Historical evaluation and future prediction of eastern North American and western Atlantic extratropical cyclones in the CMIP5 models during the cool season. *J. Climate*, **26**, 6882–6903, doi:10.1175/JCLI-D-12-00498.1.

Davis, C. A., 1992: A potential-vorticity diagnosis of the importance of initial structure and condensational heating in observed extratropical cyclones. *Mon. Wea. Rev.*, **120**, 2409–2428, doi:10.1175/1520-0493(1992)120<2409:APVDOT>2.0.CO;2.

——, M. T. Stoelinga, and Y.-H. Kuo, 1993: The integrated effect of condensation in numerical simulations of extratropical cyclogenesis. *Mon. Wea. Rev.*, **121**, 2309–2330, doi:10.1175/1520-0493(1993)121<2309:TIEOCI>2.0.CO;2.

Dee, D. P., and Coauthors, 2011: The ERA-Interim reanalysis: Configuration and performance of the data assimilation system. *Quart. J. Roy. Meteor. Soc.*, **137**, 553–597, doi:10.1002/qj.828.

Donat, M. G., G. C. Leckebusch, J. G. Pinto, and U. Ulbrich, 2010: Examination of wind storms over Central Europe with respect to circulation weather types and NAO phases. *Int. J. Climatol.*, **30**, 1289–1300, doi:10.1002/joc.1982.

Emanuel, K. A., M. Fantini, and A. J. Thorpe, 1987: Baroclinic instability in an environment of small stability to slantwise moist convection. Part I: Two-dimensional models. *J. Atmos. Sci.*, **44**, 1559–1573, doi:10.1175/1520-0469(1987)044<1559:BIIAEO>2.0.CO;2.

Farrell, B. F., 1982: The initial growth of disturbances in baroclinic flows. *J. Atmos. Sci.*, **39**, 1663–1686, doi:10.1175/1520-0469(1982)039<1663:TIGODI>2.0.CO;2.

Feser, F., M. Barcikowska, O. Krueger, F. Schenk, R. Weisse, and L. Xia, 2015: Storminess over the North Atlantic and northwestern Europe—A review. *Quart. J. Roy. Meteor. Soc.*, **141**, 350–382, doi:10.1002/qj.2364.

Frierson, D. M. W., 2007: The dynamics of idealized convection schemes and their effect on the zonally averaged tropical circulation. *J. Atmos. Sci.*, **64**, 1959–1976, doi:10.1175/JAS3935.1.

——, I. M. Held, and P. Zurita-Gotor, 2006: A gray-radiation aquaplanet moist GCM. Part I: Static stability and eddy scales. *J. Atmos. Sci.*, **63**, 2548–2566, doi:10.1175/JAS3753.1.

Graff, L. S., and J. H. LaCasce, 2014: Changes in cyclone characteristics in response to modified SSTs. *J. Climate*, **27**, 4273–4295, doi:10.1175/JCLI-D-13-00353.1.

Grise, K. M., and L. M. Polvani, 2014: The response of midlatitude jets to increased CO_2: Distinguishing the roles of sea surface temperature and direct radiative forcing. *Geophys. Res. Lett.*, **41**, 6863–6871, doi:10.1002/2014GL061638.

Hall, N. M. J., B. J. Hoskins, P. J. Valdes, and C. A. Senior, 1994: Storm tracks in a high-resolution GCM with doubled carbon dioxide. *Quart. J. Roy. Meteor. Soc.*, **120**, 1209–1230, doi:10.1002/qj.49712051905.

Held, I. M., 1993: Large-scale dynamics and global warming. *Bull. Amer. Meteor. Soc.*, **74**, 228–241, doi:10.1175/1520-0477(1993)074<0228:LSDAGW>2.0.CO;2.

Hill, K. A., and G. M. Lackmann, 2011: The impact of future climate change on TC intensity and structure: A downscaling approach. *J. Climate*, **24**, 4644–4661, doi:10.1175/2011JCLI3761.1.

Hoskins, B. J., and K. I. Hodges, 2002: New perspectives on the Northern Hemisphere winter storm tracks. *J. Atmos. Sci.*, **59**, 1041–1061, doi:10.1175/1520-0469(2002)059<1041:NPOTNH>2.0.CO;2.

——, M. E. McIntyre, and A. W. Robertson, 1985: On the use and significance of isentropic potential vorticity maps. *Quart. J. Roy. Meteor. Soc.*, **111**, 877–946, doi:10.1002/qj.49711147002.

Kidston, J., S. M. Dean, J. A. Renwick, and G. K. Vallis, 2010: A robust increase in the eddy length scale in the simulation of future climates. *Geophys. Res. Lett.*, **37**, L03806, doi:10.1029/2009GL041615.

Knippertz, P., U. Ulbrich, and P. Speth, 2000: Changing cyclones and surface wind speeds over the North Atlantic and Europe in a transient GHG experiment. *Climate Res.*, **15**, 109–122, doi:10.3354/cr015109.

Knutti, R., and J. Sedlacek, 2013: Robustness and uncertainties in the new CMIP5 climate model projections. *Nat. Climate Change*, **3**, 369–373, doi:10.1038/nclimate1716.

Kuo, Y.-H., M. A. Shapiro, and E. G. Donall, 1991: The interaction between baroclinic and diabatic processes in a numerical simulation of a rapidly intensifying extratropical marine cyclone. *Mon. Wea. Rev.*, **119**, 368–384, doi:10.1175/1520-0493(1991)119<0368:TIBBAD>2.0.CO;2.

Lackmann, G. M., 2002: Cold-frontal potential vorticity maxima, the low-level jet, and moisture transport in extratropical cyclones. *Mon. Wea. Rev.*, **130**, 59–74, doi:10.1175/1520-0493(2002)130<0059:CFPVMT>2.0.CO;2.

——, and R. M. Yablonsky, 2004: The importance of the precipitation mass sink in tropical cyclones and other heavily precipitating systems. *J. Atmos. Sci.*, **61**, 1674–1692, doi:10.1175/1520-0469(2004)061<1674:TIOTPM>2.0.CO;2.

Lambert, S. J., and J. C. Fyfe, 2006: Changes in winter cyclone frequencies and strengths simulated in enhanced greenhouse warming experiments: Results from the models participating in the IPCC diagnostic exercise. *Climate Dyn.*, **26**, 713–728, doi:10.1007/s00382-006-0110-3.

Li, M., T. Woolings, K. Hodges, and G. Masato, 2014: Extratropical cyclones in a warmer, moister climate: A recent Atlantic analogue. *Geophys. Res. Lett.*, **41**, 8594–8601, doi:10.1002/2014GL062186.

Lu, J., G. Chen, and D. M. W. Frierson, 2010: The position of the midlatitude storm track and eddy-driven westerlies in aquaplanet AGCMs. *J. Atmos. Sci.*, **67**, 3984–4000, doi:10.1175/2010JAS3477.1.

Ludwig, P., J. G. Pinto, M. Reyers, and S. L. Gray, 2014: The role of anomalous SST and surface fluxes over the southeastern North Atlantic in the explosive development of windstorm Xynthia. *Quart. J. Roy. Meteor. Soc.*, **140**, 1729–1741, doi:10.1002/qj.2253.

Marciano, C. G., G. M. Lackmann, and W. A. Robinson, 2015: Changes in U.S. east coast cyclone dynamics with climate change. *J. Climate*, **28**, 468–484, doi:10.1175/JCLI-D-14-00418.1.

Merlis, T. M., and T. Schneider, 2009: Scales of linear baroclinic instability and macroturbulence in dry atmospheres. *J. Atmos. Sci.*, **66**, 1821–1833, doi:10.1175/2008JAS2884.1.

Murray, R. J., and I. Simmonds, 1991: A numerical scheme for tracking cyclone centres from digital data. Part I: Development and operation of the scheme. *Aust. Meteor. Mag.*, **39**, 155–166.

Neu, U., and Coauthors, 2013: IMILAST: A community effort to intercompare extratropical cyclone detection and tracking algorithms. *Bull. Amer. Meteor. Soc.*, **94**, 529–547, doi:10.1175/BAMS-D-11-00154.1.

O'Gorman, P. A., 2010: Understanding the varied response of the extratropical storm tracks to climate change. *Proc. Natl. Acad. Sci. USA*, **107**, 19 176–19 180, doi:10.1073/pnas.1011547107.

——, 2011: The effective static stability experienced by eddies in a moist atmosphere. *J. Atmos. Sci.*, **68**, 75–90, doi:10.1175/2010JAS3537.1.

——, and T. Schneider, 2008a: Energy of midlatitude transient eddies in idealized simulations of changed climates. *J. Climate*, **21**, 5797–5806, doi:10.1175/2008JCLI2099.1.

——, and ——, 2008b: The hydrological cycle over a wide range of climates simulated with an idealized GCM. *J. Climate*, **21**, 3815–3832, doi:10.1175/2007JCLI2065.1.

——, and ——, 2009: Scaling of precipitation extremes over a wide range of climates simulated with an idealized GCM. *J. Climate*, **22**, 5676–5685, doi:10.1175/2009JCLI2701.1.

Pfahl, S., and H. Wernli, 2012: Quantifying the relevance of cyclones for precipitation extremes. *J. Climate*, **25**, 6770–6780, doi:10.1175/JCLI-D-11-00705.1.

Pinto, J. G., U. Ulbrich, G. C. Leckebusch, T. Spangehl, M. Reyers, and S. Zacharias, 2007: Changes in storm track and cyclone activity in three SRES ensemble experiments with the ECHAM5/MPI-OM1 GCM. *Climate Dyn.*, **29**, 195–210, doi:10.1007/s00382-007-0230-4.

Pithan, F., and T. Mauritsen, 2014: Arctic amplification dominated by temperature feedbacks in contemporary climate models. *Nat. Geosci.*, **7**, 181–184, doi:10.1038/ngeo2071.

Plant, R. S., G. C. Craig, and S. L. Gray, 2003: On a threefold classification of extratropical cyclogenesis. *Quart. J. Roy. Meteor. Soc.*, **129**, 2989–3012, doi:10.1256/qj.02.174.

Raible, C. C., P. M. Della-Marta, C. Schwierz, H. Wernli, and R. Blender, 2008: Northern Hemisphere extratropical cyclones: A comparison of detection and tracking methods and different reanalyses. *Mon. Wea. Rev.*, **136**, 880–897, doi:10.1175/2007MWR2143.1.

Reed, R. J., M. T. Stoelinga, and Y.-H. Kuo, 1992: A model-aided study of the origin and evolution of the anomalously high potential vorticity in the inner region of a rapidly deepening marine cyclone. *Mon. Wea. Rev.*, **120**, 893–913, doi:10.1175/1520-0493(1992)120<0893:AMASOT>2.0.CO;2.

Roebber, P. J., 1984: Statistical analysis and updated climatology of explosive cyclones. *Mon. Wea. Rev.*, **112**, 1577–1589, doi:10.1175/1520-0493(1984)112<1577:SAAUCO>2.0.CO;2.

——, and M. R. Schumann, 2011: Statistical analysis and updated climatology of explosive cyclones. *Mon. Wea. Rev.*, **139**, 2776–2789, doi:10.1175/MWR-D-10-05002.1.

Rossa, A. M., H. Wernli, and H. C. Davies, 2000: Growth and decay of an extra-tropical cyclones PV-tower. *Meteor. Atmos. Phys.*, **73**, 139–156, doi:10.1007/s007030050070.

Sanders, F., and J. R. Gyakum, 1980: Synoptic-dynamic climatology of the "bomb." *Mon. Wea. Rev.*, **108**, 1589–1606, doi:10.1175/1520-0493(1980)108<1589:SDCOT>2.0.CO;2.

Schemm, S., H. Wernli, and L. Papritz, 2013: Warm conveyor belts in idealized moist baroclinic wave simulations. *J. Atmos. Sci.*, **70**, 627–652, doi:10.1175/JAS-D-12-0147.1.

Schneider, T., 2007: The thermal stratification of the extratropical troposphere. *The Global Circulation of the Atmosphere*, T. Scheider and A. H. Sobel, Eds., Princeton University Press, 47–77.

——, P. A. O'Gorman, and X. J. Levine, 2010: Water vapor and the dynamics of climate changes. *Rev. Geophys.*, **48**, RG3001, doi:10.1029/2009RG000302.

Smith, K. S., 2007: The geography of linear baroclinic instability in Earth's oceans. *J. Mar. Res.*, **65**, 655–683, doi:10.1357/002224007783649484.

Stoelinga, M. T., 1996: A potential vorticity–based study of the role of diabatic heating and friction in a numerically simulated baroclinic cyclone. *Mon. Wea. Rev.*, **124**, 849–874, doi:10.1175/1520-0493(1996)124<0849:APVBSO>2.0.CO;2.

Ulbrich, U., G. C. Leckebusch, and J. G. Pinto, 2009: Extratropical cyclones in the present and future climate: A review. *Theor. Appl. Climatol.*, **96**, 117–131, doi:10.1007/s00704-008-0083-8.

——, and Coauthors, 2013: Are greenhouse gas signals of northern hemisphere winter extra-tropical cyclone activity dependent on the identification and tracking algorithm? *Meteor. Z.*, **22**, 61–68, doi:10.1127/0941-2948/2013/0420.

Wallace, J. M., G.-H. Lim, and M. L. Blackmon, 1988: Relationship between cyclone tracks, anticyclone tracks, and baroclinic waveguides. *J. Atmos. Sci.*, **45**, 439–462, doi:10.1175/1520-0469(1988)045<0439:RBCTAT>2.0.CO;2.

Wernli, H., and C. Schwierz, 2006: Surface cyclones in the ERA-40 dataset (1958–2001). Part I: Novel identification method and global climatology. *J. Atmos. Sci.*, **63**, 2486–2507, doi:10.1175/JAS3766.1.

Willison, J., W. A. Robinson, and G. M. Lackmann, 2013: The importance of resolving mesoscale latent heating in the North Atlantic storm track. *J. Atmos. Sci.*, **70**, 2234–2250, doi:10.1175/JAS-D-12-0226.1.

Yin, J. H., 2005: A consistent poleward shift of the storm tracks in simulations of 21st century climate. *Geophys. Res. Lett.*, **32**, L18701, doi:10.1029/2005GL023684.

Zappa, G., L. C. Shaffrey, K. I. Hodges, P. G. Sansom, and D. B. Stephenson, 2013: A multimodel assessment of future projections of North Atlantic and European extratropical cyclones in the CMIP5 climate models. *J. Climate*, **26**, 5846–5862, doi:10.1175/JCLI-D-12-00573.1.